Host autophagy mediates organ wasting and nutrient mobilization for tumor growth

Rojyar Khezri [1,2], Petter Holland[1,2] * Todd Andrew Schoborg[3]*, Ifat Abramovich[4], Szabolcs Takats[1,2], Caroline Dillard[1,2], Ashish Jain[1,2], Fergal OFarrell[1,2], Sebastian Wolfgang Schultz [1,2], William M. Hagopian[5], Eduardo Martin Quintana [1,2], Rachel Ng[3], Nadja Sandra Katheder[2,6,7], Mohammed Mahidur Rahman[1,2], Andreas Brech[1,2], Heinrich Jasper[6,7], Nasser M. Rusan[3] , Anne Hope Jahren[5], Eyal Gottlieb[4] and Tor Erik Rusten [1,2]

1. Centre for Cancer Cell Reprogramming, Institute of Clinical Medicine, Faculty of Medicine, 10 University of Oslo, Montebello, N-0379 Oslo, Norway.

2. Department of Molecular Cell Biology, Institute for Cancer Research, Oslo University Hospital, 13 Montebello, N-0379 Oslo, Norway. Electronic address: t.e.rusten@medisin.uio.no.

3. Cell Biology and Physiology Center, National Heart, Lung and Blood Institute, National 16 Institutes of Health, Bethesda MD 20892, USA

4. The Ruth and Bruce Rappaport Faculty of Medicine, Technion - Israel Institute of Technology, 1 Efron Street, Bat Galim, Haifa, Israel.

5. Centre for Earth Evolution and Dynamics, University of Oslo, Blindern, N-0315 Oslo, Norway

6. Buck Institute for Research on Aging, 8001 Redwood Boulevard, Novato, CA, 94945-1400, 24 USA

7. Immunology Discovery, Genentech, Inc., 1 DNA Way, South San Francisco, California 94080, 27 USA.

* These authors contributed equally to this work.

All figures contain hyperlinks for full resolution figures.

42 **During tumor growth - when nutrient and anabolic demands are high –**
43 **autophagy supports tumor metabolism and growth through lysosomal**
44 **organelle turnover and nutrient recycling** [1]**. Ras-driven tumors additionally**
45 **invoke non-autonomous autophagy in the microenvironment to support tumor**
46 **growth, in part through transfer of amino acids** [2-4]**. Here we uncover a third**
47 **critical role of autophagy in mediating systemic organ wasting and nutrient**
48 **mobilization for tumor growth using a well-characterized malignant tumor**
49 **model in** *Drosophila melanogaster***. Micro-computed X-ray tomography and**
50 **metabolic profiling reveal that** *Ras^{V12}; scrib$^{-/-}$* **tumors grow 10-fold in volume,**
51 **while systemic organ wasting unfolds with progressive muscle atrophy, loss of**
52 **body mass, -motility, -feeding and eventually death. Tissue wasting is found to**
53 **be mediated by autophagy and results in host mobilization of amino acids and**
54 **sugars into circulation. Natural abundance Carbon 13 tracing demonstrates**
55 **that tumor biomass is increasingly derived from host tissues as a nutrient**
56 **source as wasting progresses. We conclude that host autophagy mediates**
57 **organ wasting and nutrient mobilization that is utilized for tumor growth.**

58

59 **Introduction**

60

61 **Gradual organ atrophy and weight loss ensues during malignant tumor growth**
62 To assess the dynamics of organ atrophy at the whole-animal level, we adopted
63 computed tomography (CT), the gold standard for evaluating adipose and muscle
64 atrophy in cancer patients. Genetically induced GFP-labeled malignant *Ras^{V12}; scrib$^{-/-}$*
65 eye tumors grow and invade the neighboring Central Nervous System (CNS),
66 extend the larval stage and kill the host by day 10-12 [5,6]. We optimized a fixation and
67 staining protocol for high resolution micro-CT (μ-CT) imaging of developmentally
68 staged larvae [7]. This enabled ready identification, segmentation and calculation of
69 tumor and organ volumes (Fig. 1a-c Supplementary Video 1-7) [7] *Ras^{V12}; scrib$^{-/-}$*
70 tumors grow 10-fold in volume while invading and enveloping the brain from day 6 to
71 10 (Fig. 1c, Supplementary Video 7, quantified in 2a). Conversely, total larval muscle
72 volume is initially similar to control animals carrying benign *Ras^{V12}* tumors, and
73 progressively shrink by approximately 50% from day 6 to day 10 (Fig. 1b, quantified
74 in 2b). The fat body, which perform adipose and liver functions, displayed a striking
75 increase in translucency and lipid droplet size (Fig. 2e, Fig 3c) in *Ras; scrib$^{-/-}$* tumor-

76 carrying animals from day 8 [8], although fat body volume remained unaltered (Fig.

77 2d). Organ wasting and tumor growth was accompanied by approximately 35% dry

78 weight loss and a progressive loss of motility and feeding from day 8 (Fig. 2f-h). We

79 established that muscle and fat body changes can be imaged and quantified in intact

80 heat-killed whole larvae using a myosin heavy chain-GFP muscle reporter and

81 backlight microscopy (Fig 3a-c, Expanded View Fig. 1a-c). Ras^{V12}; $scrib^{-/-}$ tumors

82 inhibit ecdysone synthesis and offset the normal pupation at day 6 due to dilp8

83 secretion from tumor tissue [9,10]. No muscle or adipose tissue atrophy was observed

84 in day 10 animals where secretion of the molting hormone ecdysone was specifically

85 obliterated in *ecdysoneless* ($ecd^{1-/-}$) mutants, or by genetic elimination of the

86 ecdysone-producing prothoracic gland cells (Expanded View Fig. 1d-f). Thus, the

87 onset of muscle and adipose tissue wasting Ras^{V12}, $scrib^{-/-}$ larvae precede the

88 reduction of feeding and reduced motility, arguing together that the wasting

89 responses are not a simple function of reduced food intake or extended larval stage.

90

91 **Systemic autophagy mediates organ wasting**

92 Earlier work showed that larvae carrying Ras^{V12}; $scrib^{-/-}$ malignant tumors, but not

93 Ras^{V12} benign tumors display a systemic autophagy stress response in muscle, gut

94 and fat body [4]. To validate these finding we assessed autophagic activity using the

95 autophagy flux reporter mCherry-Atg8a. Increased lysosomal processing of mCherry-

96 Atg8a was observed in host tissues of larvae carrying Ras^{V12}; $scrib^{-/-}$ tumors from day

97 6 to 8 (Expanded View Fig. 2a) indicating an escalation in systemic tissue autophagy

98 in this model as tumor growth proceeds. Increased autophagy alongside proteasomal

99 turnover may be responsible for proteolysis and muscle atrophy. We therefore asked

100 whether autophagy is involved in organ wasting. The autophagy initiation complex

101 Atg13/Atg1/FIP200 and Atg14-containing PIK3-C3 lipid kinase complex

102 (Atg14/Vps15/Vps34/Atg6), act sequentially during autophagy initiation. As expected,

103 fully mutant *atg13* animals carrying Ras^{V12}; $scrib^{-/-}$ tumors, did not display autophagy

104 flux and instead accumulated the autophagy cargo protein Ref(2)P/p62 (Expanded

105 View Fig. 2a). Strikingly, Ras^{V12}; $scrib^{-/-}$, $atg13^{-/-}//atg13^{-/-}$ animals displayed a

106 complete reversal of muscle atrophy, weight and motility loss, as well as fat body

107 alterations (Fig. 3a-d, f-h, Expanded View Fig. 2b,c, Supplementary video 8,9).

108 Genomic rescue of *atg13* (*g-atg13*) in Ras^{V12}; $scrib^{-/-}$, $atg13^{-/-}//atg13^{-/-}$ animals

109 reinstated organ wasting, showing that the failure of organ wasting was indeed due to

110   *atg13* loss (Expanded View Fig. 2d,e). *Ras^V12; scrib^-/-, atg14^-//atg14^-/-* animals also

111   blocked organ wasting and loss of motility, demonstrating that failure of organ

112   wasting is not limited to the autophagy initiation complex (Expanded View Fig. 2f-g).

113   Importantly, as *Ras^V12; scrib^-/-, atg13^-//atg13^-/-* also show reduced tumor growth, we

114   rescued tumor growth by local *atg13* expression in the tumor and microenvironment

115   of the eye-antennal disc only. This led to rescue of tumor growth to 60% as

116   previously reported, but failed to cause systemic atrophy, (Fig. 3e, f-h). Thus,

117   systemic autophagy drives organ wasting and tumor growth is dependent upon local

118   as well as systemic autophagy.

119

120   **Autophagy mediates nutrient mobilization**

121   Autophagy mediates nutrient recycling upon starvation at the cell level through

122   lysosomal turnover and recycling of lipids, sugars, amino acids and nucleotides that

123   may further be secreted into circulation [1,11,12]. We therefore investigated whether

124   autophagy can mediate systemic nutrient release in this model. The levels of

125   metabolites in the cell free hemolymph (serum) were measured using LC/MS

126   analysis.

127   Serum levels of amino acids; arginine, proline, glutamine, serine, alanine, lysine as

128   well as the insect serum sugar, trehalose, were significantly increased in animals with

129   *Ras^V12; scrib^-/-* tumors relative to age-matched controls (Fig. 4a). This was apparent

130   already at day 6, before onset of significant and exponential tumor growth and

131   reduced feeding. Conversely, glutamate and methionine were lower (Fig. 4a). By day

132   8, serum amino acid and trehalose levels increased further, including glutamate and

133   methionine before tapering off at day 10 while glucose peaked (Fig. 4a, Expanded

134   View Fig 3a). Thus, serum nutrient levels increase during organ atrophy suggesting

135   that autophagy may mediate nutrient release into circulation. To test this, we

136   compared *Ras^V12; scrib^-/-* tumor-carrying animals with and without autophagy.

137   Trehalose, arginine, glutamine, proline, tyrosine, serine and asparagine showed

138   significant higher levels in autophagy-competent *Ras^V12; scrib^-/-* animals versus

139   *atg13*-mutant *Ras^V12; scrib^-/-* tumor carrying animals at day 6 (Fig. 4b) and this was

140   followed by the majority of amino acids except tyrosine at day 8 (Expanded View Fig.

141   3a). This supports the hypothesis that autophagy is required for increased serum

142   nutrient levels in tumor-ridden animals. Indeed, we could not detect significant

143   differences in serum nutrient levels between *Ras^V12; scrib^-/-, atg13^-//atg13^-/-* and

144   *Ras^{V12}*control animals at day 6 (Expanded View Fig. 3b). In order to infer which

145   metabolites are changed early on during organ wasting in an autophagy-dependent

146   manner, we performed three pairwise comparisons at day 6. Metabolites that

147   increased significantly (FDR < 0.05) upon wasting 1) Ras^{V12};scrib$^{-/-}$ vs Ras^{V12},

148   reversed when autophagy was inhibited 2) Ras^{V12};scrib$^{-/-}$ Atg13$^{-/-}$ vs Ras^{V12};scrib$^{-/-}$

149   and not altered in autophagy mutants alone 3) Ctrl Atg13$^{-/-}$ vs Ctrl. This set of criteria

150   identified arginine, asparagine, glutamine, proline, and trehalose to respond early

151   and strong at the onset of muscle wasting (Fig. 4c).

152   In flies, autophagy cooperates with enzymatic breakdown of muscle glycogen

153   via glycogen phosphorylase in response to starvation, raising the possibility that

154   autophagy may contribute to glycogen breakdown and serum sugar mobilization [13].

155   Visualizing glycogen by immunofluorescence staining in muscle and fat body, or

156   biochemically measuring total tissue sugar showed that glycogen stores are depleted

157   in day 8 *Ras^{V12}, scrib$^{-/-}$* animals relative to day 6 while serum trehalose levels rise

158   (Fig. 5a-e, Fig. 4c). Both glycogen stores and trehalose levels normalized in *Ras^{V12};*

159   *scrib$^{-/-}$, atg13$^{-/-}$//atg13$^{-/-}$* animals (Fig. 5a-e and Expanded View Fig 3c). Taken

160   together, this provides *in vivo* evidence that autophagy mediates somatic organ

161   wasting and mobilization of nutrients in the form of sugars and amino acids and that

162   mobilization initiates before reduced feeding and onset of exponential tumor growth.

163

164

165   **Host-derived nutrients constitute the main source of tumor biomass**

166   These findings raised the tantalizing possibility that autophagy mediates nutrient

167   release from host tissues that may further be utilized by the tumor for growth. To test

168   this hypothesis, we sought to differentiate whether biomass of the growing tumor was

169   derived from ingested food or nutrients released from host organ stores. As both

170   sugars and amino acids were mobilized as a group, we chose to follow transfer of

171   carbon using natural abundance Stable Isotope Ratio Mass Spectrometry (SIRMS)

172   using a recently developed protocol [14] . We generated two types of fly food

173   containing different $^{13}C/^{12}C$ ratios derived from plants with differences in ^{13}C vs ^{12}C

174   incorporation from CO_2 during photosynthesis. C4–type carbon fixation (e.g. corn,

175   sugar cane) incorporates relatively more ^{13}C-containing CO_2 than does C3-type

176   plants (e.g. potato, sugar beet) [14-16]. Larvae raised on C4-based vs C3-based food

177   revealed segregated $^{13}C/^{12}C$ values in keeping with the isotopic composition of the

178 food they were raised on (Expanded View Fig 4a). To measure incorporation of
179 carbon from different sources into the growing tumor, we switched the food source 25
180 hours before measuring the isotopic carbon ratio as well as total carbon mass of the
181 cephalic complex. The measured change in mass and carbon composition during
182 those 25 hours then reveal the relative amount of carbon that has been added to the
183 tumor from ingested food or host organs. We find that early tumor growth sources a
184 majority of biomass carbon from the food, but that carbons are increasingly
185 incorporated from the host tissues as tumor growth progresses (Fig 5f, g, Expanded
186 View Fig 4b).

187

188

189

190

191 **Discussion**

192 Earlier studies in adult flies have demonstrated ovary atrophy in adult flies carrying
193 allografted Ras^{V12}; $scrib^{-/-}$ or Ras^{V12};$dlg^{-/-}$ tumors derived from the larval eye disc or
194 in animals with adult stem cell tumors in the gut driven by defective Hippo-Warts
195 signaling. Ovary atrophy is mediated by IMPL2, an insulin-binding peptide produced
196 by the tumor. Muscles showed altered mitochondrial morphology, but muscle wasting
197 was not reported in either model. Detailed μ–CT and volumetric calculations
198 presented here demonstrate that muscle wasting occurs in response to Ras^{V12}; $scrib^{-/-}$
199 , but that the fat body volume is retained with increased signs of steatosis. Muscle
200 wasting was also reported to be induced by fibroblast growth factor secretion in a
201 Ras^{V12}, Csk-IR larval model while this paper was being revised [17]. In both models, a
202 concomitant increase in amino acid serum levels is observed raising the question of
203 what is the mechanism for nutrient mobilization.

204   Autophagy captures intracellular material and delivers it to the lysosome for
205 degradation and recycling of amino acids, sugars, fatty acids and nucleotides to
206 sustain metabolism and enable survival during starvation in mice and flies [18]. It is well
207 established that autophagy is required in tumor cells to uphold tumor cell metabolism
208 and mitochondrial functionality cell intrinsically. More recently, non-autonomous
209 effects of autophagy in cancer progression have been revealed. In mouse and
210 *Drosophila*, *Ras*-driven tumors stimulate neighboring cells of the microenvironment to
211 activate autophagy to support tumor growth [2,4]. Pancreatic stellate cells secrete

212 asparagine and alanine in response to tumor cells and alanine taken up by the tumor
213 was shown to functionally support tumor growth by entering central TCA metabolism
214 [2]. Beyond the microenvironment, systemic depletion of autophagy leads to strong
215 decline in serum arginine due to the release of arginase from the liver that in turn
216 restricts growth of arginine-auxotrophic tumors [19]. Whether autophagy may have a
217 broader effect on physiology and tumor growth when cancer leads to systemic organ
218 wasting is so far unknown. The results herein support a model where autophagy
219 supports tumor growth from peripheral tissues in a fly model [4]. As autophagy
220 mediates massive nutrient release, we favor a model in which autophagy supports
221 tumor growth by bulk nutritional provisioning through amino acid and sugar
222 mobilization. This is supported by measurements showing that biomass increase is
223 mainly derived from host carbon sources in this model. We cannot rule out other
224 autophagy-mediated mechanisms that may also support growth and that the tumor is
225 opportunistically incorporating the released molecules. Given the similarities between
226 human cancer cachexia processes and the findings presented herein, autophagy
227 inhibition may also be an effective way to mitigate symptoms of cachexia and
228 increase quality of life. [18]
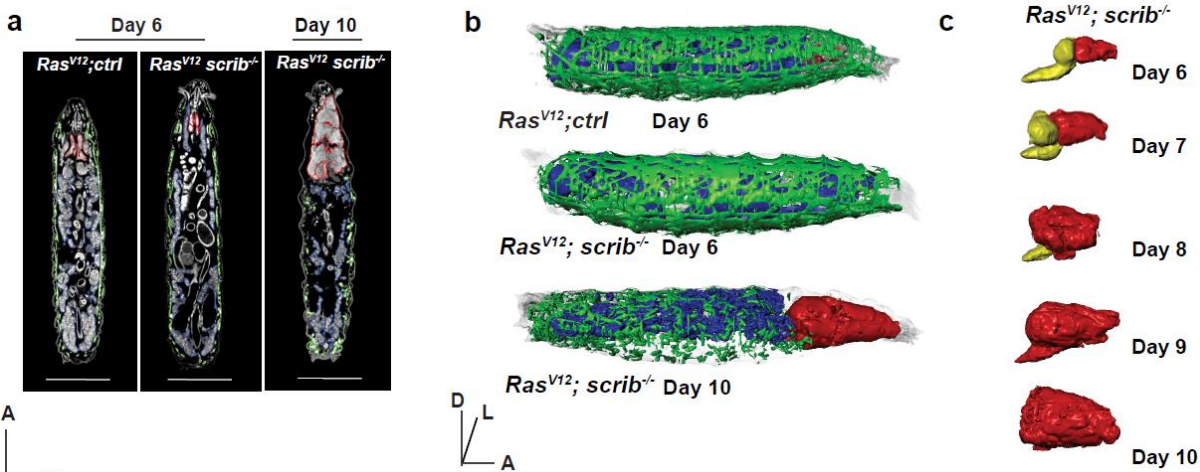229 .

Figure Legends

Figure 1. **Tumor induced organ wasting**. **(a)** Representative 2D μ-CT scans of Ras^{V12}; ctrl at day 6, Ras^{V12}; scrib$^{-/-}$ larvae at day 6 and day 10. Muscle (green), fat body (blue) and eye-antennal discs/tumor (red) are outlined. **(b)** Representative 3D rendering of genotypes indicated in (a). Anterior (A), Dorsal (D), Left (L), Right (R). **(c)** Representative 3D rendering of Ras^{V12}; scrib$^{-/-}$ tumors (red) and central nervous system (yellow), over time.
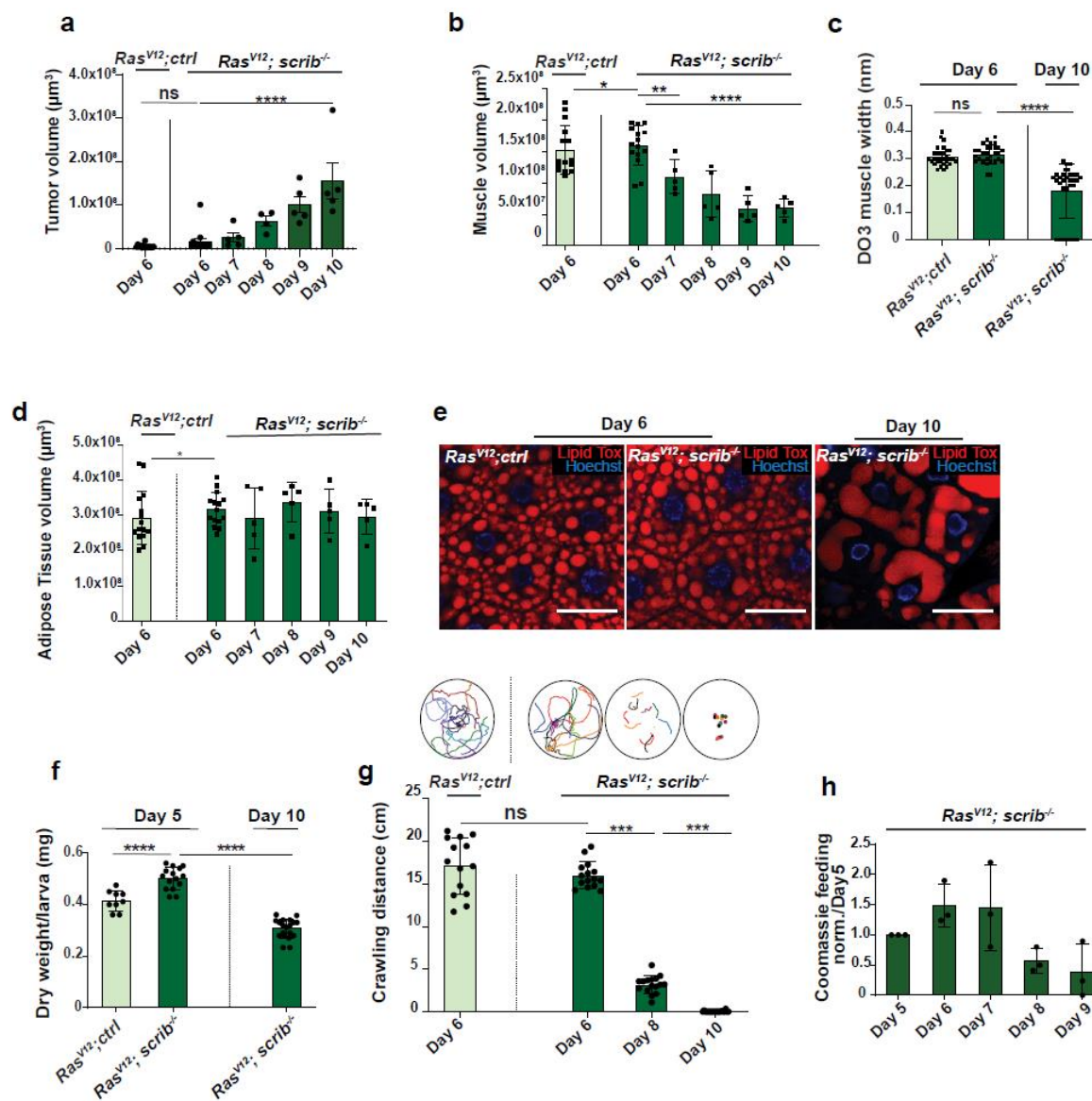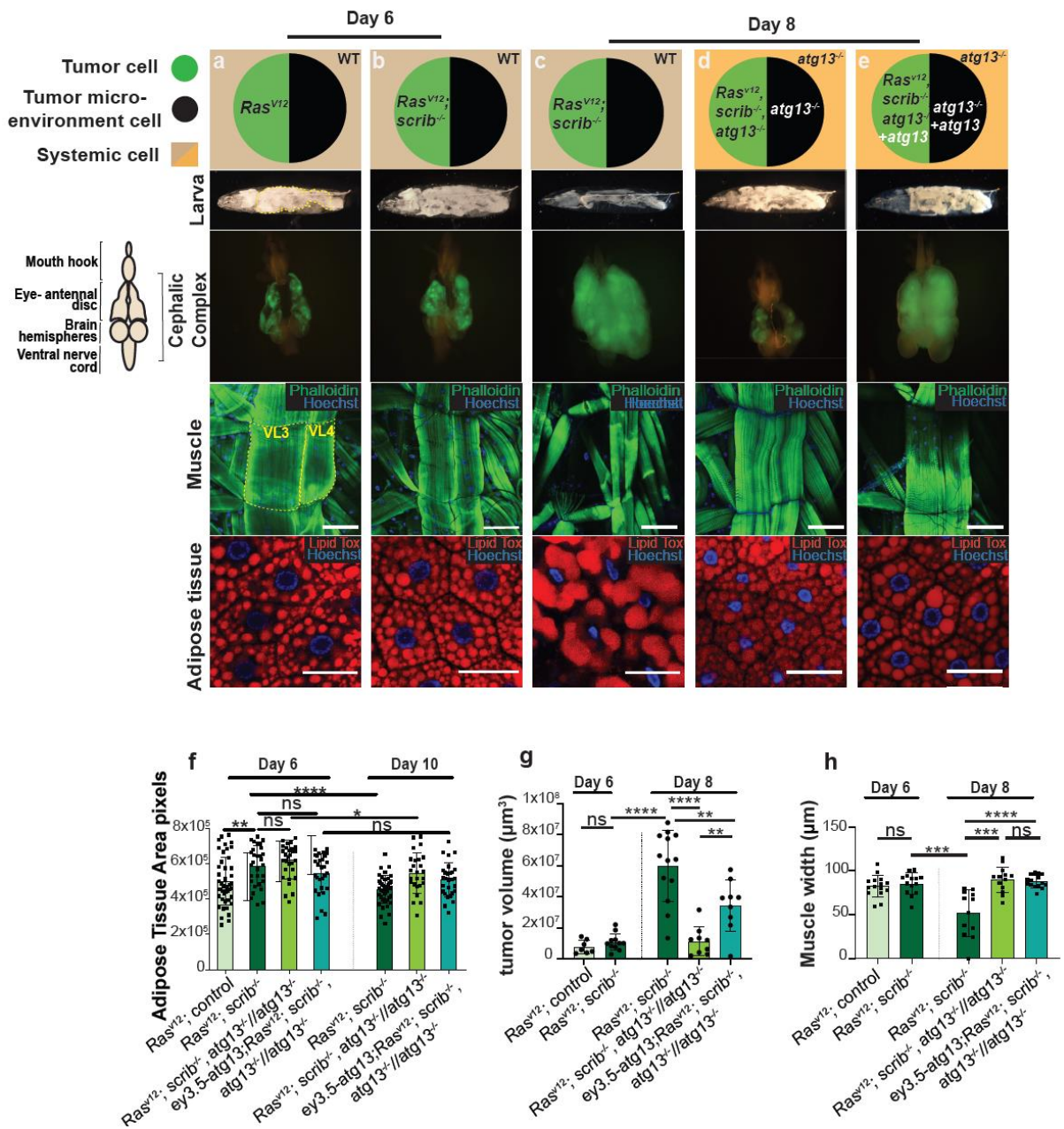
Figure 2. **Tumor induced organ wasting. (a)** Quantification of tumor growth of Ras^{V12}; ctrl day 6 (n=15) Ras^{V12}; scrib$^{-/-}$ tumors, day 6 (n=15), day 7 (n=5), day 8 (n=4), day 9 (n=5) and day 10 (n=5). **(b)** Quantifications of muscle volume, of larvae carrying tumors of Ras^{V12}; ctrl (n=15), and Ras^{V12}; scrib$^{-/-}$ at day 6(n=15), day 7 (n=5), day 8 (n=5), day 9 (n=5) and dat 10 (n=5). **(c)** Quantification of width of Dorsal Oblique 3 (DO3) muscle in larvae carrying tumors of Ras^{V12}; ctrl at day 6 (n=29) and Ras^{V12}; scrib$^{-/-}$at days 6 (n=29) and day 10 (n=31). **(d)** Quantification of adipose tissue volume in larvae carrying tumors of Ras^{V12}; ctrl at day 6 and Ras^{V12}; scrib$^{-/-}$at days 6 and day 10. **(e)** Representative confocal images of adipose tissue in Ras^{V12}; ctrl and Ras^{V12}; scrib$^{-/-}$ tumors bearing animals at indicated ages. Lipid droplets are highlighted with Lipid Tox staining. **(f)** Quantification of dry weight of Ras^{V12}; ctrl (n=9), Ras^{V12}; scrib$^{-/-}$ day 6(n=15) and day 10(n=18) tumor bearing larvae excluding

252   the tumor weight. **(g)** Quantification of larval motility measure by crawling distance

253   and crawling pattern in *Ras^{V12}; ctrl* (n=14), *Ras^{V12}; scrib$^{-/-}$* day 6 (n=15), day 8 (n=16)

254   and day 10(n=14), each colored line represents a single larva. **(h)** Coomassie

255   feeding assay to asses food intake of *Ras^{V12}; scrib$^{-/-}$* over time, three repeated

256   measurements of an average food intake of 20 larvae. Values depict mean±s.e.m. of

257   minimum three independent pooled experiments. ns, not significant, *$P \leq 0.05$, **$P \leq$

258   0.01, ***$P \leq 0.0001$ and ****$P < 0.0001$, from unpaired, two-tailed test. Scale bar:

259   (1a): 1mm, (1h):50 μm.

260

261

262

Figure 3. **Autophagy is required for systemic wasting.** Cartoon (top) illustrates the genotypes of the larvae, eye-antennal disc (EAD, circle: tumor cells in green and microenvironment cell in black), systemic cells are illustrated as a square (wild type cells in light brown and *atg13* mutant cells in light orange) at indicated ages. Cartoon (left) illustrates the structure of cephalic complex attached to mouth hook. Representative images of Larva (image of larva using the backlight of microscope), cephalic complex (green highlights the GFP-labelled tumor clones), muscle (Phalloidin in green stains actin and Hoechst in blue stains nucleus) and adipose tissue (Lipid Tox in red stains for lipid droplets, Hoechst stains nucleus) from top to

272   bottom. (**a**) *Ras^{V12}; ctrl* tumor bearing animal at day 6. (**b**) *Ras^{V12}; scrib$^{-/-}$* tumor

273   bearing animal at day 6. (**c**) *Ras^{V12}; scrib$^{-/-}$* tumor bearing animal at day 8. (**d**) *Ras^{V12},*

274   *scrib$^{-/-}$, atg13$^{-/-}$//atg13$^{-/-}$* at day 8. (**e**) *Ras^{V12}, scrib$^{-/-}$, atg13$^{-/-}$//atg13$^{-/-}$* animal

275   complemented with transgenic *atg13*, rescuing the tumor growth, at day 8. (**f**)

276   Quantification of area of space occupied with lobes of fat body within larval segments

277   4 to 8 (shown in yellow dashed line in 2a), of animals bearing tumors at day 6 *Ras^{V12};*

278   *ctrl* (n=45)*, Ras^{V12}; scrib$^{-/-}$* (n=30), *Ras^{V12}, scrib$^{-/-}$, atg13$^{-/-}$//atg13$^{-/-}$* (n=30) and *ey3.5-*

279   *atg13; Ras^{V12}, scrib$^{-/-}$, atg13$^{-/-}$//atg13$^{-/-}$* (n=29) and at day 10 *Ras^{V12}; scrib$^{-/-}$* (n=40),

280   *Ras^{V12}, scrib$^{-/-}$, atg13$^{-/-}$//atg13$^{-/-}$* (n=25) and *ey3.5-atg13; Ras^{V12}, scrib$^{-/-}$, atg13$^{-/-}$*

281   *//atg13$^{-/-}$* (n=28). (**g**) Quantification of tumor volumes day 6 *Ras^{V12}; ctrl* (n=7)*, Ras^{V12};*

282   *scrib$^{-/-}$* (n=11) and day 8 *Ras^{V12}; scrib$^{-/-}$* (n=13), *Ras^{V12}, scrib$^{-/-}$, atg13$^{-/-}$//atg13$^{-/-}$* (n=9)

283   and *ey3.5-atg13; Ras^{V12}, scrib$^{-/-}$, atg13$^{-/-}$//atg13$^{-/-}$* (n=9). (**h**) Quantification of Ventral

284   Longitudinal muscle 4 (VL4) (shown in yellow dashed line in 2a) of third segment of

285   larvae carrying at day 6 *Ras^{V12}; ctrl* (n=15)*, Ras^{V12}; scrib$^{-/-}$* (n=14), and at day8

286   *Ras^{V12}; scrib$^{-/-}$* (n=11), *Ras^{V12}, scrib$^{-/-}$, atg13$^{-/-}$//atg13$^{-/-}$* (n=12) and *ey3.5-atg13;*

287   *Ras^{V12}; scrib$^{-/-}$, atg13$^{-/-}$//atg13$^{-/-}$* (n=14). (**i**) Quantification of dry weight excluding

288   tumor of *Ras^{V12}; scrib$^{-/-}$, atg13$^{-/-}$//atg13$^{-/-}$* at day 6 (n=8) and day 10 (n=7). (**j**)

289   Quantification of larval motility measured by crawling distance and crawling pattern

290   for *Ras^{V12}; scrib$^{-/-}$, atg13$^{-/-}$//atg13$^{-/-}$* at day 6 (n=15) and at day 8 (n=15), each colored

291   line represents a single larva. Values depict mean±s.e.m. of minimum three

292   independent pooled experiments. ns, not significant, *$*P \leq 0.05$, $**P \leq 0.01$, $***P \leq$*

293   *0.0001* and *$****P < 0.0001$*, from unpaired, two-tailed test. Scale bar: muscles 100
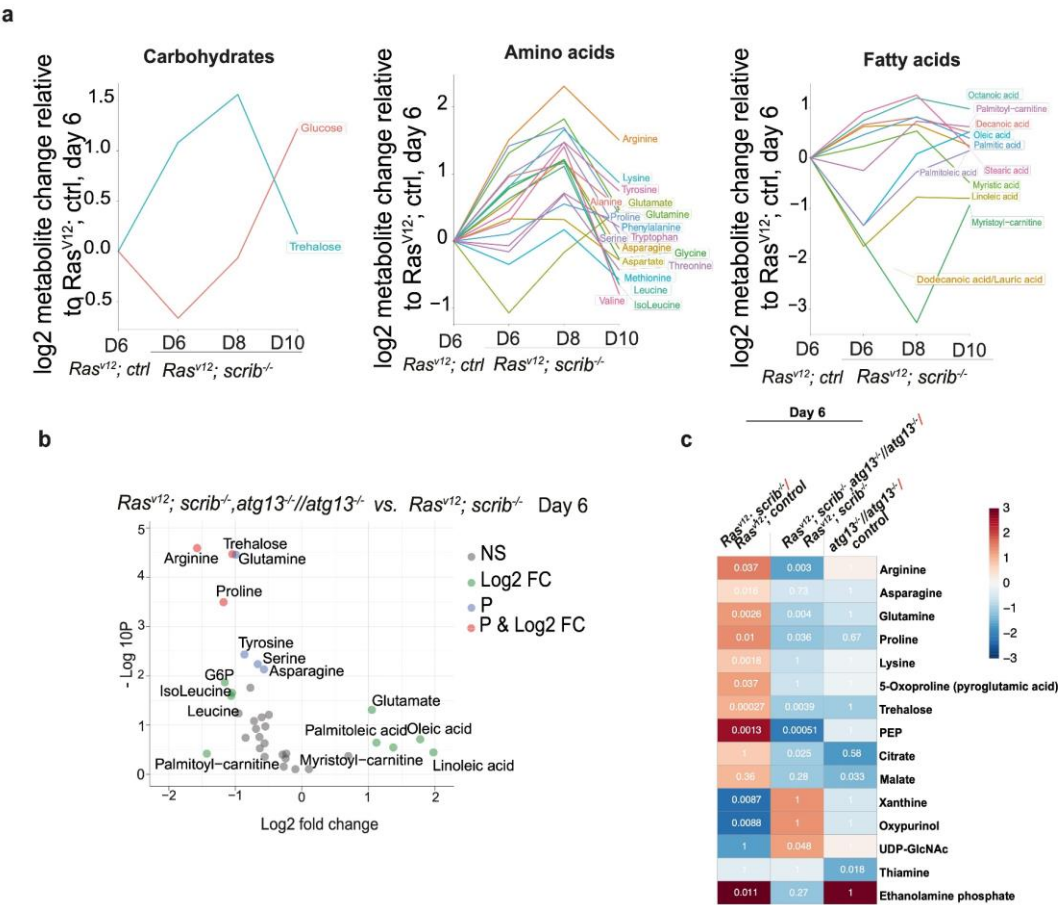
294   μm and adipose tissue 50 μm.

295

296

297

Figure 4. **Autophagy-driven wasting releases metabolites into circulation. (a)** Changes in groups (carbohydrates, amino acids and fatty acids) of storage metabolites measured in circulating haemolymph with progressing wasting, shown as log2 changes measured by LC-MS and calculated per larvae relative to Ras^{V12}; ctrl at day 6. **(b)** Volcano plot showing autophagy-dependent changes to amounts of circulating metabolites at day 6. X-axis shows the log2 of fold change of Ras^{V12};atg13 $^{-/-}$scrib$^{-/-}$ // atg13 $^{-/-}$ vs. Ras^{V12}; scrib$^{-/-}$, y-axis shows -log10 p-value, calculated by t-test. Metabolite names are shown for metabolites with log2(FC) >± 1 and/or -log10(P) < 2. Green points indicate log2(FC) >± 1, blue indicate -log10(P) < 2 and red indicates for above both thresholds. **(c)** Autophagy-driven wasting releases metabolites into circulationof 113 reliably detected metabolites, those showing significant differences in any of the three comparisons are shown. Color indicates the log2(fold change) difference and the numbers show the p-value of the comparison. The statistical test to define significance was FDR-adjusted t-test p-value < 0.05
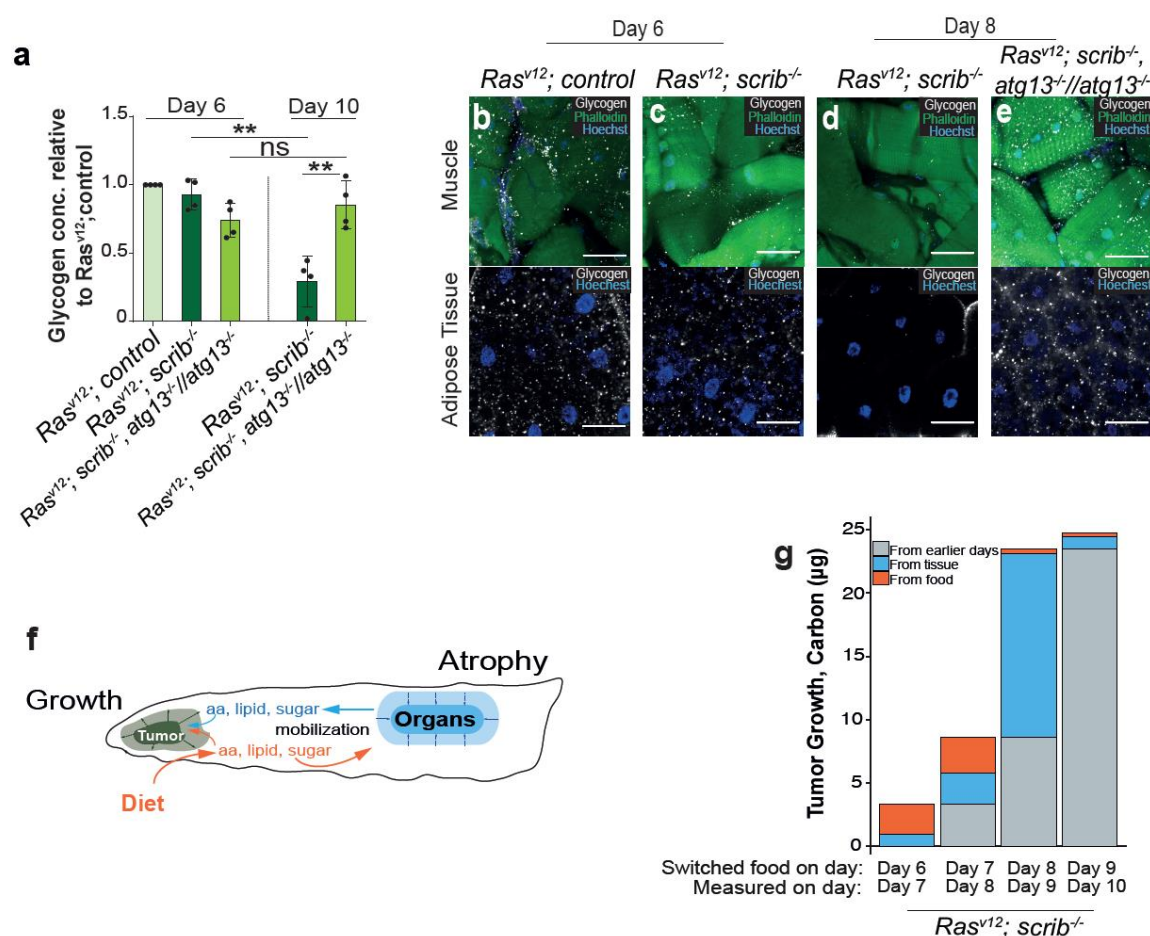
Figure 5. Host-derived nutrients contribute to tumor biomass. **(a)** The amount of glycogen in the whole larvae measured by biochemical assay (n=4), normalized to *Ras^{V12}; ctrl* at day 6, and per number of larvae. **(b-e)** Representative confocal images of muscle and adipose tissue of larvae carrying *Ras^{V12}; ctrl*, *Ras^{V12}; scrib$^{-/-}$* and *Ras^{V12}; scrib$^{-/-}$, atg13$^{-/-}$//atg13$^{-/-}$* showing glycogen levels (white) at day 6 and day 8. (f) Cartoon illustrating tumor growth (green) incorporation of molecules derived from food (in orange) or from host tissues (in blue). **(g)** Sources of carbon incorporated into tumor biomass were differentiated by changing the isotopic carbon content of the food source 25 hours before measuring the total carbon content and isotopic ratio of the tumor. Values depict mean±s.e.m. of minimum three independent pooled experiments. ns, not significant, *$P \leq 0.05$, **$P \leq 0.01$ and ****$P < 0.0001$, from unpaired, two-tailed test. Scale bar: muscles 100 μm and adipose tissue 50 μm.

331

332

333

334

335
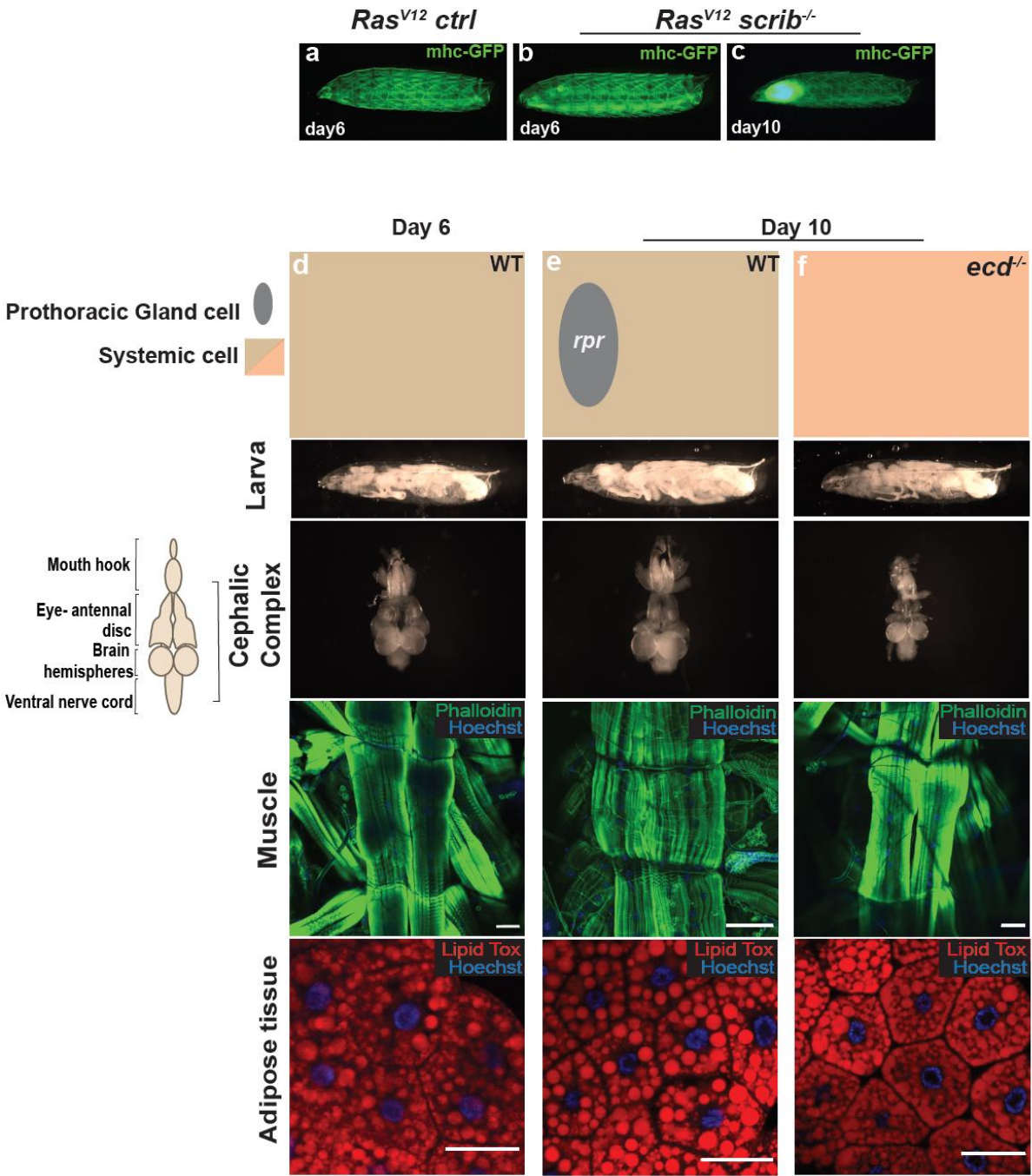
Expanded View Figure 1. Tumor-induced organ wasting. (a-c) Representative images of larvae with GFP-labelled muscles at day 6 and 10. **(d-f)** Cartoon (top) illustrates the genotypes of the larvae, prothoracic gland (grey oval), systemic cells are illustrated as a square (wild type cells in light brown and ecdysone mutant cells in

340   light red) at day 6 and day 10. Cartoon (left) illustrates the structure of cephalic

341   complex attached to mouth hook. Larva (image of larva using the backlight of

342   microscope), cephalic complex (no tumors), muscle (Phalloidin in green stains actin

343   and Hoechst in blue stains muscle nuclei) and adipose tissue (Lipid Tox in red stains

344   for lipid droplets, Hoechst stains cell nuclei) from top to bottom. **(d)** Wild type larva

345   (w^{1118}) control, **(e)** spok-Gal4,UAS-Dcr2.D;UAS-rpr larva that linger due to lack of

346   cells expressing ecdysone hormone and **(f)** ecd^{1ts} (ecdysoneless), larva that lingers

347   due to ecdysone deficiency. Scale bar: muscle, 100 μm and adipose tissue, 50μm.

348

349

350
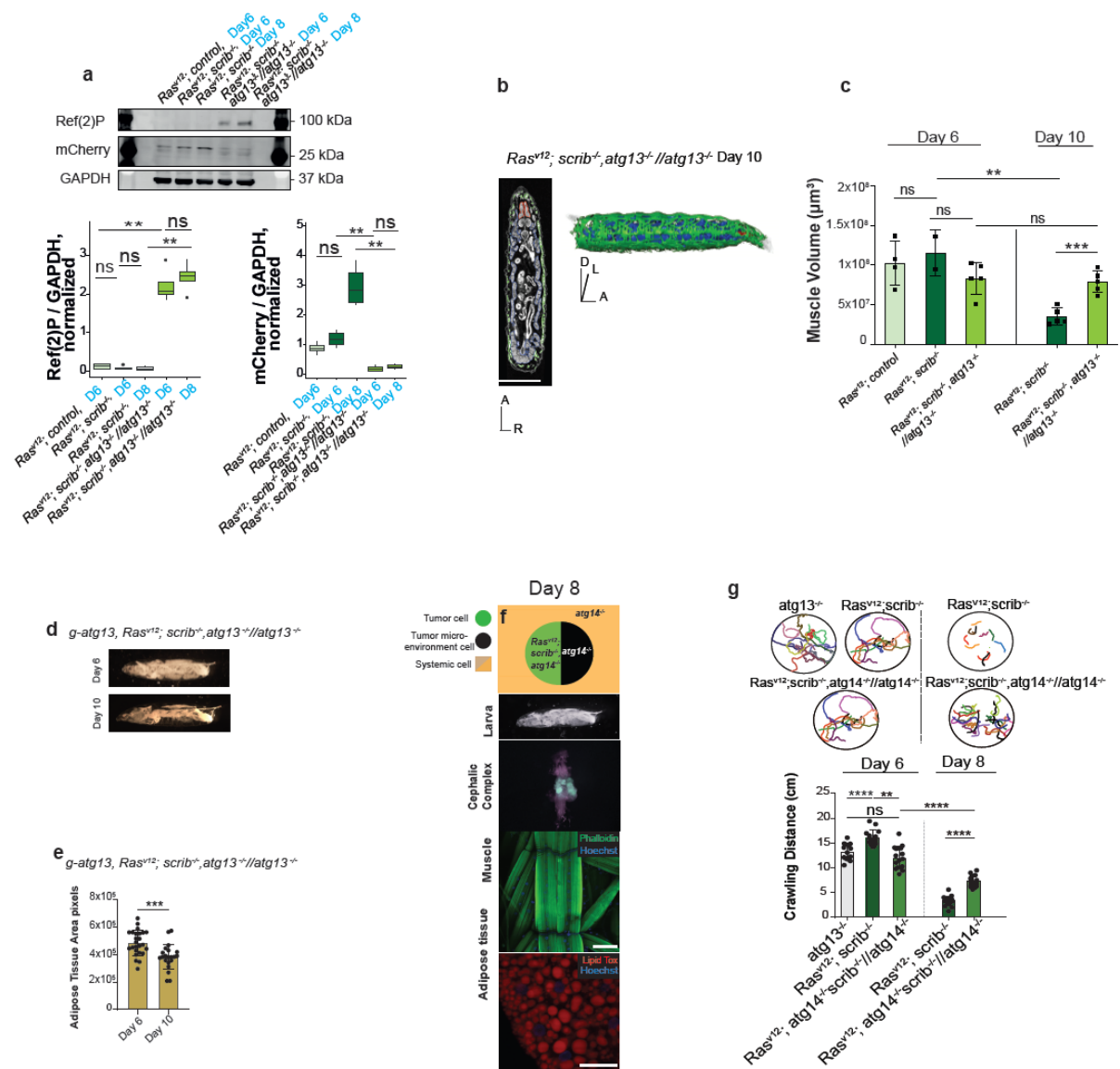
Expanded View Figure 2. Autophagy is required for systemic wasting. (a) Western blot analysis and quantification of Cherry-Atg8a processing and Ref(2)P accumulation in larval body wall muscles, representative of four independent experiments. Quantifications are normalized to the mean of signals for a given band in each independent experiment. **(b)** Representative 2D μ-CT scan and representative 3D rendering of of Ras^{V12}; $scrib^{-/-}$, $atg13^{-/-}//atg13^{-/-}$ larva at day 10. Muscle (green), fat body (blue) and eye-antennal discs/tumor (red), Anterior (A), Dorsal (D), Left (L), Right (R). **(c)** Quantifications of muscle volumes larvae carrying at day 6 Ras^{V12}; $ctrl$ (n=4), Ras^{V12}; $scrib^{-/-}$ (n=2), Ras^{V12}; $scrib^{-/-}$, $atg13^{-/-}//atg13^{-/-}$ (n=5) and at day 10 Ras^{V12}; $scrib^{-/-}$ (n=5), Ras^{V12}; $scrib^{-/-}$, $atg13^{-/-}//atg13^{-/-}$ (n=5). **(d)** Representative images of whole larva at days 6 and 10 of $g\text{-}atg13$, Ras^{V12}; $scrib^{-/-}$, $atg13^{-/-}//atg13^{-/-}$ **(e)** Quantification of space within segments 4-8 occupied by white

364   adipose tissue in a whole/intact larva, shown in pixels **(f)** Cartoon (top) illustrates the

365   genotypes of the larva, eye-antennal disc (EAD, circle: tumor cells in green and

366   microenvironment cell in black), systemic cells are illustrated as a square.

367   Representative images of Ras^{V12}; $scrib^{-/-}$, $atg14^{-/-}//atg14^{-/-}$larva (image of larva using

368   the backlight of microscope), cephalic complex (green highlights the GFP-labelled

369   tumor clones), muscle (Phalloidin in green stains actin and Hoechst in blue stains

370   nucleus) and adipose tissue (Lipid Tox in red stains for lipid droplets, Hoechst stains

371   nucleus) from top to bottom. **(g)** Quantification of larval motility measured by crawling

372   distance and crawling pattern for $atg13^{-/-}$ larvae (n=12), Ras^{V12}; $scrib^{-/-}$ (same data

373   that shown in Figure 2.) Ras^{V12}; $scrib^{-/-}$, $atg14^{-/-}//atg14^{-/-}$ at day 6 (n=15) and at day 8

374   (n=16), each colored line represents a single larva. Values depict mean±s.e.m. of

375   minimum three independent pooled experiments, (except for Exp. View Fig 2c,

376   Ras^{V12}; $scrib^{-/-}$ at day 6)   ns, not significant, $*P \leq 0.05$, $**P \leq 0.01$ and $***P \leq 0.0001$

377   or as indicated in the figure (b), from unpaired, two-tailed test. Scale bar: muscles

378   100 μm and adipose tissue 50 μm.

379

380

381
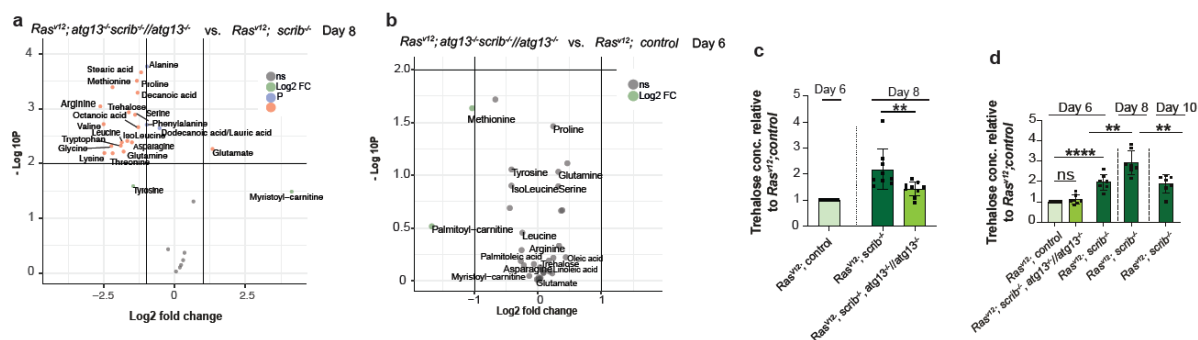
382 **Expanded View Figure 3. Autophagy-driven wasting releases metabolites into**

383 **circulation. (a)** Volcano plot showing autophagy-dependent changes to amounts of

384 circulating metabolites in wasting larvae at age 8. X-axis shows the log2 of fold

385 change of Ras^{V12}; $scrib^{-/-}$, $atg13^{-/-}//atg13^{-/-}$ vs. Ras^{V12}; $scrib^{-/-}$, y-axis shows -log10 p-

386 value, calculated by t-test. Metabolite names are shown for metabolites with log2(FC)

387 $>\pm$ 1 and/or -log10(P) < 2. Green points indicate log2(FC) $>\pm$ 1, blue indicate -

388 log10(P) < 2 and red indicates for above both thresholds. **(b)** Volcano plot showing

389 the amounts of circulating metabolites in Ras^{V12}; $scrib^{-/-}$, $atg13^{-/-}//atg13^{-/-}$ vs. Ras^{V12};

390 ctrl at day 6. **(c)** The amount of trehalose measured by biochemical assay in whole

391 larvae (n=9) in Ras^{V12}; $scrib^{-/-}$ and Ras^{V12}; $scrib^{-/-}$, $atg13^{-/-}//atg13^{-/-}$ at day 8,

392 normalized to Ras^{V12}; ctrl at day 6, and per number of larvae. (d) The amount of

393 trehalose measured by biochemical assay of the whole larvae (n=7), in Ras^{V12}; $scrib^{-/-}$

394 $^{/-}$, $atg13^{-/-}//atg13^{-/-}$ at day 6 and Ras^{V12}; $scrib^{-/-}$ at day 6, 8 and 10 normalized to

395 Ras^{V12}; ctrl at day 6, and per number of larvae.

396 Values depict mean±s.e.m. of minimum three independent pooled experiments; ns,

397 not significant, $^{**}P \leq 0.01^{**}P \leq 0.01$ and $^{****}P < 0.0001$, from unpaired, two-tailed test.

398

399

400

401

402
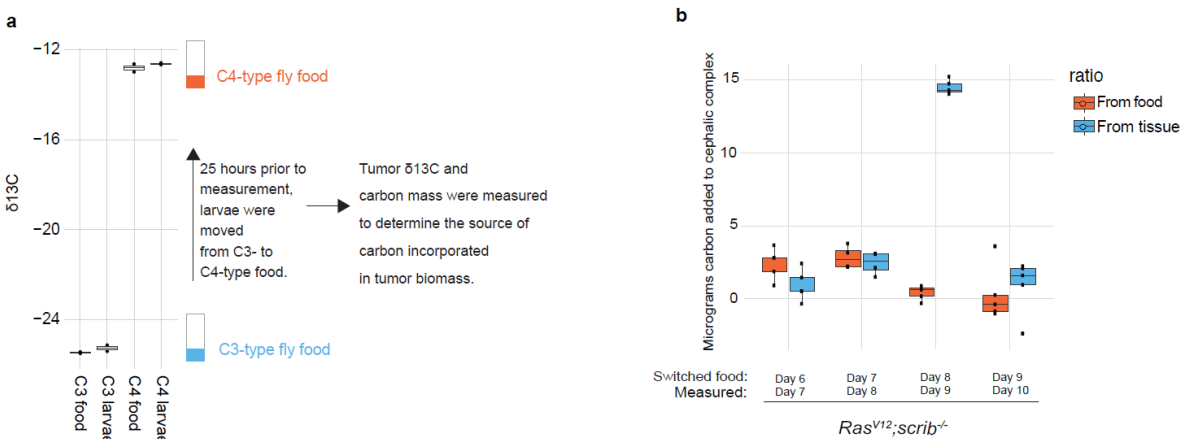
Expanded View Figure 4. Tumor incorporation of carbon isotopes. Determining the source of carbon used for tumor biomass expansion. (a) δ13C (representing 13C/12C) measurements of two different food types, either with C3- or C4-type plant-derived nutrients. Measurements of whole larvae growing on these food types for are also shown along with a brief description of the methodology to determine the source of carbon used for tumor growth. Two measurements are shown for all samples. (b) Carbon incorporated into the cephalic complex biomass from food or host tissues were determined by moving RasV12; scrib-/- larvae at indicated stages tumor development from C3- to C4-type food and then measuring the carbon composition as well as carbon mass 25 hours later.

413

414

415

416

417

Supplementary files

VIDEOS

Supplementary Video 1. 2D μ-CT scan of a *Ras^{V12}; ctrl* larva at Day 6, showing the entire range of projection images acquired from two different perspectives. Muscle (green), fat body (blue) and eye-antennal discs/tumor (red) are outlined. *Top:* Movie begins at the right side of the larva and moves towards the left side. *Bottom:* Movie begins at the dorsal surface and moves towards the ventral surface (top to bottom). Scale Bar: 1mm; Anterior (A), Dorsal (D), Right (R).

Supplementary Video 2. 2D μ-CT scan of a *Ras^{V12}; scrib$^{-/-}$* larva at Day 6, showing the entire range of projection images acquired from two different perspectives. Muscle (green), fat body (blue) and eye-antennal discs/tumor (red) are outlined. *Top:* Movie begins at the right side of the larva and moves towards the left side. *Bottom:* Movie begins at the dorsal surface and

Supplementary Video 3. 2D μ-CT scan of a *Ras^{V12}; scrib$^{-/-}$* larva at Day 10, showing the entire range of projection images acquired from two different perspectives. Muscle (green), fat body (blue) and eye-antennal discs/tumor (red) are outlined. *Top:* Movie begins at the right side of the larva and moves towards the left side. *Bottom:* Movie begins at the dorsal surface and moves towards the ventral surface (top to bottom). Scale Bar: 1mm; Anterior (A), Dorsal (D), Left (L).

Supplementary Video 4. 3D rendering of *Ras^{V12}; ctrl* larva at Day 6 showing muscle (green), fat body (blue) and eye disc/tumor (red). Movie begins at the right side of the larva and clips towards the left side before reversing direction. Movies towards the ventral surface (top to bottom). Scale Bar: 1mm; Anterior (A), Dorsal (D), Right (R).

Supplementary Video 5. 3D rendering of *Ras^{V12}; scrib$^{-/-}$* larva at Day 6 showing muscle (green), fat body (blue) and eye disc/tumor (red). Movie begins at the right side of the larva and clips towards the left side before reversing direction.

452

453

Supplementary Video 6. 3D rendering of Ras^{V12}; $scrib^{-/-}$ larva at Day 10 showing muscle (green), fat body (blue) and eye disc (red). Movie begins at the right side of the larva and clips towards the left side before reversing direction.

457

Supplementary Video 7. 3D rendering of Ras^{V12}; $scrib^{-/-}$ larva tumor (red) and central nerve system (yellow). Movie shows the growth of tumor in time, through day 6 to day 10.

461

462

Supplementary Video 8. 2D μ-CT scan of a Ras^{V12}; $scrib^{-/-}$ larva at Day 10 (top) and Ras^{V12}; $scrib^{-/-}$, $atg13^{-/-}//atg13^{-/-}$ larva at Day 10 (bottom), showing the entire range of projection images acquired. Muscle (green), fat body (blue) and eye-antennal discs/tumor (red) are outlined. Movie begins at the dorsal surface and moves towards the ventral surface (top to bottom). Scale Bar: 1mm; Anterior (A), Right (R).

468

Supplementary Video 9. 3D rendering of Ras^{V12}; $scrib^{-/-}$ larva at Day 10 (top) and Ras^{V12}; $scrib^{-/-}$, $atg13^{-/-}//atg13^{-/-}$ larva at Day 10 (bottom) showing muscle (green), fat body (blue) and eye disc/tumor (red). Movie begins at the right side of the larva and clips towards the left side before reversing direction. Anterior (A), Dorsal (D), Left (L).

473

474

475

476

477

478

479 **Materials and methods**

480 Fly Husbandry and fly food

481 Stocks and crosses were kept at 25 °C on standard potato mash fly food containing

482 32.7 g dried potato powder, 60 g sucrose, 27.3 g dry yeast, 7.3 g agar, 4.55 ml

483 propionic acid, and 2 g nipagin per liter, resulting in a final concentration of 15.3 g

484 l^{-1} protein and 6 g l^{-1} sugar, unless otherwise indicated. Additional yeast paste was

485 added to the vials.

486

487 Temperature sensitive crosses (Figure 4c-h), were set up in 18°C on standard fly

488 food. Third instar larval stage L2 larvae were collected and transferred to 30 °C

489 incubator for induction of selected genes, under the temperature sensitive promoter.

490

491 Immunofluorescence staining and microscopy

492 Larval cephalic complexes, muscles and fat bodies were dissected in PBS and fixed

493 in PBS containing 4% paraformaldehyde for 30 min at room temperature. Samples

494 were washed twice with PBS and blocked with PBT (PBS containing 0.1% Triton X-

495 100 and 3% BSA). Primary antibody was incubated over night at +4°C, followed by

496 two washes with and secondary antibodies, incubated at room temperature for 1h.

497 Tissue samples were washed and mounted in Vectashield mounting medium (H-

498 1000) and observed with a Zeiss LSM 710 or LSM 780 confocal microscope.

499 Hoechst 33342 (Life technologies, H3570, final concentration 5 μg ml^{-1}) and Alexa

500 Fluor-488/647 Phalloidin (H3572, 1:200) were added to stain nuclei and actin,

501 respectively and Lipid Tox Red (Thermo Fisher Scientific, 1:1000). Antibodies used in

502 this study: antiglycogen monoclonal glycogen antibody (1:100, mouse, IgM,

503 Generous gift from Otto Baba).

504

505 Metabolite analysis

506

507 20 larvae were washed thoroughly with cold Saline (0.9% NaCl solution), ensuring no

508 traces of food was left on the larval body wall. Larvae were dried completely of saline

509 solution by placing them on Kim Tech paper wipes. Larvae were then transferred into

510   pre-cooled 0.5 ml microcentrifuge tube with a 3-4 mm cut at the bottom center
511   vertically, one by one and using forceps tip a hole was made into the head region of
512   the larva, avoiding puncturing the tumor or the gut. The 0.5 ml microcentrifuge tube
513   was then transferred into a pre-cooled 1.5 ml microcentrifuge tube and centrifuged at
514   1000 x g for 1 min at 4°C for hemolymph extraction. Tube containing the larval
515   carcasses was removed and extracted hemolymph solution was re-centrifuged at
516   *1000 x g, for 5 min* at 4°C for the removal of hemocytes. 5 µl of serum was pipetted
517   into a new pre-cooled microcentrifuge tube avoiding the hemocytes in the bottom,
518   followed by immediate addition of 70µl of the extraction solvent (LC-MS methanol 75
519   %: LC-MS acetonitrile 25%, Merck, containing labelled standards, Metabolomic QC
520   Kit for Untargeted/Targeted Mass Spectrometry, A Cambridge Isotope Laboratories
521   Company). The solution was mixed well for 5 min. at 4°C. Sample solutions were
522   centrifuged at 14 000 rpm, for 10 min at 4°C. The supernatant was moved into a new
523   Eppendorf tube and kept at -80°C until analysis. LC-MS metabolomics analysis was
524   performed as_described previously [20]. Briefly, Thermo Ultimate 3000 high-
525   performance liquid chromatography (HPLC) system coupled to Q- Exactive Orbitrap
526   Mass Spectrometer (Thermo Fisher Scientific) was used with a resolution of 35,000
527   at 200 mass/charge ratio (*m/z*), electrospray ionization, and polarity switching mode
528   to enable both positive and negative ions across a mass range of 67 to 1000 *m/z*.
529   HPLC setup consisted ZIC-pHILIC column (SeQuant; 150 mm x 2.1 mm, 5 µm;
530   Merck), with a ZIC-pHILIC guard column (SeQuant; 20 mm x 2.1 mm). 5 ul of
531   Biological extracts were injected and the compounds were separated with mobile
532   phase gradient of 15 min, starting at 20% aqueous (20 mM ammonium carbonate
533   adjusted to pH 9.2 with 0.1% of 25% ammonium hydroxide) and 80% organic
534   (acetonitrile) and terminated with 20% acetonitrile. Flow rate and column temperature
535   were maintained at 0.2 ml/min and 45°C, respectively, for a total run time of 27 min.
536   All metabolites were detected using mass accuracy below 5 ppm. Thermo Xcalibur
537   was used for data acquisition

538

539   TraceFinder 4.1 was used for analysis. Peak areas of metabolites were determined
540   by using the exact mass of the singly charged ions. The retention time of metabolites
541   was predetermined on the pHILIC column by analyzing an in-house mass
542   spectrometry metabolite library consisting of commercially available standards. For
543   data normalization, raw data files were processed with Compound Discoverer 3.0 to

544   obtain total compounds peak area for each sample. Each metabolite peak area value

545   analyzed in the sample was normalized to total measurable ions in the sample.

546

547

548   For further calculations, the ion counts measured by the LC-MS were imported to R

549   (R Core Team, 2019). From the concentration/metabolites peak area that were

550   measured on the LC-MS instrument, the normalized total amount of each metabolite

551   in circulation per larvae was calculated by multiplying by the hemolymph volume of

552   the larvae with the peak area and dividing by the total measurable ions for that

553   sample. Peak area, volumes and total measured ions for all samples are supplied in

554   Supplementary Data 1. To allow log2 (fold change) measurements even if there are

555   metabolites that are not detected in a sample set, all normalized total amounts were

556   added 0.0001 for the log2(fold change) calculations. P values were calculated by the

557   t.test function in R and volcano plots made by the Enhanced Volcano (Kevin Blighe,

558   2019) library in R

559

560   Trehalose measurement

561

562   Three larvae of the indicated ages were collected and washed thoroughly in cold

563   PBS three times. Larvae were then dried on a Kim Tech paper, and transferred into a

564   1.5 ml microcentrifuge tube containing ice cold lysis buffer 20 μl/larva (Pierce

565   Luciferase Cell Lysis Buffer (2X), Thermo Scientific) and immediately homogenized

566   using a pellet pestle. Samples were then heated for 10 min at 70°C, followed by

567   centrifugation at 14 000 rpm, for 10 min at 4°C. The supernatant was transferred into

568   a new 1.5 ml microcentrifuge tube.

569

570   Trehalose amount was measured using Trehalose Assay Kit (Product code: K-TREH,

571   Megazyme Ltd.) according to the manufacturer's instructions, with the exception of

572   using 20μl of larval sample extraction per 200μl of total sample volume, in 96 well

573   plate. Two aliquots were measured, with and without trehalase enzyme, to measure

574 background glucose amount and trehalose converted to glucose amount. Samples
575 were normalized to the amount of larvae and to the control sample (Ras^{V12};control).

576

577

578 Glycogen measurement

579

580 Three larvae of the indicated ages were collected and washed thoroughly in cold
581 PBS three times. Larvae were then dried on a Kim Tech paper, and transferred into a
582 1.5 ml microcentrifuge tube containing ice cold lysis buffer 30 μl/larva (Pierce
583 Luciferase Cell Lysis Buffer (2X), Thermo Scientific) and immediately homogenized
584 using a pellet pestle. Samples were then heated for 10 min at 70°C, followed by
585 centrifugation at 14 000 rpm, for 10 min at 4°C. The supernatant was transferred into
586 a new 1.5 ml microcentrifuge tube.

587

588 Glycogen amount was measured using Glycogen Colorimetric Assay Kit II (Catalog
589 #: K648, BioVision, Inc), according to the manufacturer's instructions, with the
590 exception of using 10μl of larval extract solution in the total volume of 150 μl. An
591 addition sample aliquot was measured without Hydrolysis Enzyme Mix to measure
592 the background glucose level, which was subtracted from the total glucose level
593 (background glucose + glycogen converted to glucose) to obtain glycogen only
594 amount. Samples were normalized to the amount of larvae and to the control sample
595 (Ras^{V12};control).

596

597

598 mCherry flux assay, western blot

599

600 Body wall perparations were made from three dissected larvae, added to 30 μl RIPA
601 buffer (150 mM NaCl, 50 mM Tris-HCl pH 7.5, 1% Triton X-100, 1% sodium
602 deoxycholate, 0.2% SDS) with complete protease inhibitor cocktail (Sigma,
603 11697498001). Lysates were sonicated 10 cycles of 30 seconds at high intensity
604 then debris sedimented by centrifugation 10 minutes, 18000 g at 4 °c. The cleared
605 lysates were normalized to protein content by the Pierce BCA assay kit (Thermo

606   Scientific, 23227) and 8 µg of protein was added from each sample to a 26-well

607   Criterion TGX 4-20% precast gel (Bio-rad, 5671095). Proteins were transferred to an

608   Immun-Blot low flouresence PVDF membrane (Bio-rad, 1620264) using a semi-dry

609   transfer system. Membranes were first blocked in 5% FA-free BSA for 1 hour (Sigma,

610   A7030) then incubated with primary antibodies goat anti-mCherry (Acris, AB0040-

611   200) at 1:1000, mouse anti-GAPDH (Abcam, ab9484) at 1:2500, rabbit anti-Ref(2)p

612   (generated in-house). Membranes were then washed and incubated with fluorescent

613   secondary antibodies for the appropriate species (Li-Cor) using either the 680 nm or

614   800 nm channels. Finally, membranes were washed and flourescence detected using

615   an Odyssey imaging system (Li-Cor). All membrane incubations and washes were

616   performed in PBS with 0.05% Tween-20 (Sigma, P1379). Membrane band

617   quantification was performed with ImageJ, first marking the band area by the

618   rectangle tool, creating a closed area that selects the band area while excluding any

619   surrounding noise by a straight line then selecting the rectangle by the wand tool

620   which gives the quantified band intensity.

621

622

623   Larval Locomotor Assays

624   Larval locomotor assay was conducted to measure distance travelled in the set time

625   of 4 minutes. Individual larva was carefully set on a 15 cm Petri dish containing

626   harden 2% agarose. Larval movement was tracked by drawing over the petri dish

627   cap. Larval travelled distance was measured using fiji and each line was normalized

628   to the cap diameter.

629

630   Larval Dry Weight

631

632   Glass microscopy slides were weighed on a ME54 Mettler Toledo scale. 10 larvae

633   were collected at different time points, washed 3x in water to remove any food

634   particles, dried off on Kim wipes and dissected directly on the glass slide to remove

635   the entire transformed brain complex and eye discs. Slides were allowed to dry at

636   room temperature for 24h and weighed again to determine the dry weight of the

637   animals.

638

639

640

Heat Fixation and imaging

642

Larva was collected and washed thoroughly in PBS, and transferred into a drop pf 100% glycerol on a microscope slide. To heat fix the larva the slide was placed onto a heat block at 70°C for approximately 10 sec. or until larva immobile. Overview of larval fat body and muscles (FGP-labelled myosin heavy chain (Mhc)) were obtained on a Leica MZ FLIII fluorescence stereomicroscope with a Leica DFC420 camera, using the backlight or fluorescence filters. Dissected cephalic complexes were imaged immediately in a drop of PBS similarly. For the segmentation of fat body occupied space, images were analyzed with Fiji image processing software. Background was subtracted with a rolling ball (radius 400), and images smoothened with Gaussian blur filter (sigma =2). Thresholding was then performed using the "Minimum dark" method.

654

655

656

657

Carbon Transfer measured by Stable Isotope Ratios (CATSIR)

659

C3-based food was prepared with 32.7 g/L potato mash, 60 g/L sucrose from beets and 27.3 g/L dry yeast ($\delta^{13}C$ measured to be similar to C3-type sugars). C4-based food was prepared with 32.7 g/L corn flour, 62 g/L sucrose from sugar cane and 26.3 g/L dry yeast that was expanded on sugar cane sucrose. The sugar cane and yeast content of the C4 food was adjusted to account for the slightly higher protein content and lower carbohydrate content of the corn flour compared to the potato mash, giving a similar final fat, protein and carbohydrate content of the two food variants. Both foods were also added 4.55 ml/L propionic acid (Sigma, P5561), 2 g/L nipagin (Sigma, H5501) and 7.3 g/L agar (AS Pals, 77000). When moving larvae from C3 to C4 food, holes were poked in surface of the new food to give easy access and the larvae were then left for 24+1 hours, assuming 1 hour for the previous C3 food to be absorbed or passed through the gut (Wong et al, Nature Methods, 2008). Before

672   dissection larvae were washed 3 times in water and cephalic complex was dissected

673   in a drop of ultrapure water. The cephalic complex from a single larvae was added to

674   a tin cup (Elemental microanalysis, D1006) and samples were left to dry in a

675   dessicator.

676   The $\delta^{13}C$ value and total carbon mass of each sample was determined in triplicate

677   using a Delta V Advantage Isotope Ratio Mass Spectrometer (Thermo Fisher,

678   Bremen, Germany) configured to a Thermo Finnigan 1112 Series Flash Elemental

679   Analyzer at the University of Oslo, Norway. Raw data is reported in standard δ-

680   notation (in units of permil, ‰) and normalized to the Vienna Pee Dee Belemnite

681   (VPDB) scale using three internal lab reference materials (JRICE: $\delta^{13}C$ = -27.44‰;

682   JHIST: $\delta^{13}C$ = -8.15‰; and JGLY: $\delta^{13}C$ = -43.51‰). For all samples, the median

683   standard deviation of the replicate capsules was 0.10‰.

684

685   To determine how much carbon is derived from the food or host tissues after moving

686   the larvae from one food to the other, $\delta^{13}C$ measurement of any given day were

687   compared to a set of measurements of larval cephalic complexes growing on only C3

688   or C4 food. This comparison is required because the $\delta^{13}C$ of the cephalic complex

689   with a growing tumor gradually changes as the tumor grows, as is described in more

690   detail in the method publication [14]. First, the relative ratio of carbon derived from food

691   and host was determined by comparing the measured $\delta^{13}C$ to the C3- and C4-only

692   samples. Then the measured total carbon mass of the cephalic complex was

693   multiplied by this relative ratio to determine the total carbon added from the two

694   different carbon sources.

695

696

697

698

699

700   *µ-CT*

701   *Labeling:* Third instar larvae were collected and transferred to a 1.5ml Eppendorf

702   tube containing 1 ml of 0.5% phosphate buffered saline + Triton-X 100 (0.5% PBST)

703   and incubated for 5 minutes at room temperature. Larvae were then fixed in 1 ml

704   Bouin's solution (5% acetic acid, 9% formaldehyde, 0.9% picric acid; Sigma Aldrich,

705   St. Lous, MO) for 2 hrs at room temperature. A microdissection needle was then

706   used to poke a small hole in the cuticle at both the anterior and posterior ends of

707 each larva, carefully avoiding any underlying soft tissue. This allows for better
708 penetration of the Bouin's solution and even fixation of all larval tissues. Fresh
709 Bouin's solution was then added and larvae were left to incubate another 16-22 hrs
710 at room temperature. Larvae were then washed 3x30 minutes in 1 ml of μ-CT Wash
711 Buffer (0.1M Na_2HPO_4, 1.8% Sucrose) and stained with 1 ml of a 0.1N solution of
712 iodine-iodide (I_2KI, Lugol's solution) for 1-2 days at room temperature. Larvae were
713 then washed in two changes of ultrapure water and stored at room temperature.

714 *Scanning:* Individual larva were mounted for scanning using a P10 pipet tip filled with
715 water, wedged inside a small piece of plastic capillary tube that fits tightly in a
716 custom-made brass holder. A dulled 20-gauge needle was used to gently push the
717 larva down in the pipet tip until it became wedged along the wall, which was
718 necessary to prevent sample movement during scanning. Larva were scanned using
719 a SkyScan 1172 desktop scanner controlled by Skyscan software (Bruker) operating
720 on a Dell workstation computer (Intel Xeon X5690 processor @ 3.47GHz (12 CPUs),
721 50 GB RAM and an NVIDIA Quadro 5000 (4GB available graphics memory) GPU).
722 X-Ray source voltage & current settings: 40 kilovolts (kV), 110 microamps (μA), 4
723 watts (W) of power. A Hamamatsu 10Mp camera with a 11.54 μm pixel size coupled
724 to a scintillator was used to convert X-rays to photons. Medium camera settings at an
725 image pixel size of 4.5 μm were used for fast scans (~20 minutes), which consists of
726 about 300 projection images that are acquired. Small camera settings at an image
727 pixel size of 2.5 μm and utilizing 360 degrees of sample rotation (~1500 projection
728 images) were used for the slow overnight (O/N) scans. Random movement was set
729 to 10 and frame averaging ranged from 4-8. At these settings, the scanner has a
730 measured resolution of 5.5 μm under optimal imaging conditions (Morales et al.,
731 2016). Medium camera settings (fast scans) provide enough resolution for accurate
732 morphometric analysis of tissues, whereas small camera settings (slow O/N scans)
733 provide high resolution for assessment of tissue/tumor morphology.

734 *Reconstruction:* Tomograms were generated using NRecon software (Bruker
735 MicroCT, v1.7.0.4). Reconstruction was performed using a built-in shit correction
736 algorithm that uses reference scans to correct for sample drift in the projection
737 images, followed by an iterative application of misalignment and ring artifact
738 reduction algorithms to generate the highest quality images possible (Salmon et al.,
739 2009).

740 *Image Analysis & Statistics:* Tomograms were visualized and analyzed using
741 Dragonfly (v4.1, Object Research Systems (ORS) Inc, Montreal, Canada, 2019;
742 software available at http://www.theobjects.com/dragonfly) operating on a Dell
743 workstation (Intel Xeon CPU E5-2623 @ 3.00GHz (16 CPUs), 32 GB RAM, NVIDIA
744 Quadro M2000 GPU (20 GB available graphics memory) and Dell Precision T7600
745 workstation (Intel® Xeon® CPU E5-2620 @ 2.00GHz, 32GB RAM, 64-bit Operating
746 System, 3GB NVIDIA Quadro K4000 GPU). Segmentation of anatomical structures
747 into individual regions of interest (ROIs) was performed manually using thresholded
748 images with the 3D paintbrush function. To eliminate human bias during
749 segmentation, a single threshold value was selected that encompassed the entire
750 structure of interest in all images that were to be compared. This threshold value was
751 then applied to all images and used for segmentation of tissues into ROIs. Small
752 adjustments to this threshold value for some individuals were made when necessary
753 to fully encompass a given tissue to be measured, to account for slight differences in
754 contrast (as a result of X-Ray beam fluctuations) between samples. ROIs were then
755 converted to meshes for quantitative analysis and visualization. The built-in 2D and
756 3D movie maker was used to generate all movies.

757

769

770

771 **Author Contributions:** R.K, P.H, E.G., W.M.H., A.H.J. and T.E.R. designed the
772 research; R.K., P.H., T.S., I.A., S.T., C.D., A.J., T.A.S, F.O.F., S.W.S., N.S.K, and
773 M.M.R. performed experiments and analyzed the data. E.M.Q. and R.N. performed

774   analysis of μ-CT data. A.B., H.J. and N.M.R. contributed to the conception of the

775   work. R.K., P.H. and T.E.R wrote the manuscript. T.E.R is the leading principal

776   investigator who conceived the project, supervised research and edited the paper.

777

778   The authors declare that they have now conflict of interest

779
780
781
782
783

784   References

785   1   Kimmelman, A. C. & White, E. Autophagy and Tumor Metabolism. *Cell metabolism*
786   **25**, 1037-1043, doi:10.1016/j.cmet.2017.04.004 (2017).

787   2   Sousa, C. M. *et al.* Pancreatic stellate cells support tumour metabolism through
788   autophagic alanine secretion. *Nature* **536**, 479-483, doi:10.1038/nature19084 (2016).

789   3   Yang, A. *et al.* Autophagy Sustains Pancreatic Cancer Growth through Both Cell-
790   Autonomous and Nonautonomous Mechanisms. *Cancer discovery* **8**, 276-287,
791   doi:10.1158/2159-8290.Cd-17-0952 (2018).

792   4   Katheder, N. S. *et al.* Microenvironmental autophagy promotes tumour growth.
793   *Nature* **541**, 417-420, doi:10.1038/nature20815 (2017).

794   5   Pagliarini, R. A. & Xu, T. A genetic screen in Drosophila for metastatic behavior.
795   *Science (New York, N.Y* **302**, 1227-1231 (2003).

796   6   Brumby, A. M. & Richardson, H. E. scribble mutants cooperate with oncogenic Ras or
797   Notch to cause neoplastic overgrowth in Drosophila. *The EMBO journal* **22**, 5769-
798   5779, doi:10.1093/emboj/cdg548 (2003).

799   7   Schoborg, T. A., Smith, S. L., Smith, L. N., Morris, H. D. & Rusan, N. M. Micro-
800   computed tomography as a platform for exploring Drosophila development.
801   *Development (Cambridge, England)*, doi:10.1242/dev.176685 (2019).

802   8   Figueroa-Clarevega, A. & Bilder, D. Malignant Drosophila tumors interrupt insulin
803   signaling to induce cachexia-like wasting. *Developmental cell* **33**, 47-55,
804   doi:10.1016/j.devcel.2015.03.001 (2015).

805   9   Garelli, A., Gontijo, A. M., Miguela, V., Caparros, E. & Dominguez, M. Imaginal discs
806   secrete insulin-like peptide 8 to mediate plasticity of growth and maturation. *Science*
807   *(New York, N.Y* **336**, 579-582, doi:10.1126/science.1216735 (2012).

808   10   Colombani, J., Andersen, D. S. & Leopold, P. Secreted peptide Dilp8 coordinates
809   Drosophila tissue growth with developmental timing. *Science (New York, N.Y* **336**,
810   582-585, doi:10.1126/science.1216689 (2012).

811   11   Kuma, A. *et al.* The role of autophagy during the early neonatal starvation period.
812   *Nature* **432**, 1032-1036 (2004).

813   12   Karsli-Uzunbas, G. *et al.* Autophagy is required for glucose homeostasis and lung
814   tumor maintenance. *Cancer discovery* **4**, 914-927, doi:10.1158/2159-8290.CD-14-
815   0363 (2014).

816   13   Zirin, J., Nieuwenhuis, J. & Perrimon, N. Role of autophagy in glycogen breakdown
817   and its relevance to chloroquine myopathy. *PLoS biology* **11**, e1001708,
818   doi:10.1371/journal.pbio.1001708 (2013).

819   14   Petter Holland, W. M. H., A. Hope Jahren, Tor Erik Rusten. Natural abundance
820   isotope ratios to differentiate sources of carbon used during tumor growth in vivo.
821   *bioRxiv*, doi:https://doi.org/10.1101/2020.09.22.307587 (2020).
822   15   Jahren, A. H. *et al.* An isotopic method for quantifying sweeteners derived from corn
823   and sugar cane. *Am J Clin Nutr* **84**, 1380-1384, doi:10.1093/ajcn/84.6.1380 (2006).
824   16   Chartrand, M. M. G. & Mester, Z. Carbon isotope measurements of foods containing
825   sugar: A survey. *Food Chem* **300**, 125106, doi:10.1016/j.foodchem.2019.125106
826   (2019).
827   17   Newton, H. *et al.* Systemic muscle wasting and coordinated tumour response drive
828   tumourigenesis. *Nature communications* **11**, 4653, doi:10.1038/s41467-020-18502-9
829   (2020).
830   18   Poillet-Perez, L. & White, E. Role of tumor and host autophagy in cancer metabolism.
831   *Genes & development* **33**, 610-619, doi:10.1101/gad.325514.119 (2019).
832   19   Poillet-Perez, L. *et al.* Autophagy maintains tumour growth through circulating
833   arginine. *Nature* **563**, 569-573, doi:10.1038/s41586-018-0697-7 (2018).
834   20   Mackay, G. M., Zheng, L., van den Broek, N. J. & Gottlieb, E. Analysis of Cell
835   Metabolism Using LC-MS and Isotope Tracers. *Methods Enzymol* **561**, 171-196,
836   doi:10.1016/bs.mie.2015.05.016 (2015).
837

Detailed genotypes

Figure 1.

1a-c: *y,w,ey-FLP/y,w;UAS-Ras^{V12}/act>y^{+}>GAL4, UAS-GFP; Frt82B/Frt82B, tub-GAL80*

y,w,ey-FLP/y,w;UAS-Ras^{V12}/act>y^{+}>GAL4, UAS-GFP; Frt82B, scrib^{1}/Frt82B, tub-GAL80

Figure 2.

1a-h: *y,w,ey-FLP/y,w;UAS-Ras^{V12}/act>y^{+}>GAL4, UAS-GFP; Frt82B/Frt82B, tub-GAL80*

y,w,ey-FLP/y,w;UAS-Ras^{V12}/act>y^{+}>GAL4, UAS-GFP; Frt82B, scrib^{1}/Frt82B, tub-GAL80

Figure 3.

3a: *y,w,ey-FLP/y,w;UAS-Ras^{V12}/act>y^{+}>GAL4, UAS-GFP; Frt82B/Frt82B, tub-GAL80*

3b,c: *y,w,ey-FLP/y,w;UAS-Ras^{V12}/act>y^{+}>GAL4, UAS-GFP; Frt82B, scrib^{1}/Frt82B, tub-GAL80*

3d: *y,w,ey-FLP/y,w;UAS-Ras^{V12}/act>y^{+}>GAL4, UAS-GFP; Frt82B, atg13$^{\Delta81}$scrib^{1}/Frt82B, tub-GAL80, atg13$^{\Delta81}$*

3e: *y,w,ey-FLP/ ey3.5-Hsp70-DmAtg13-GFP;UAS-Ras^{V12}/ act>y^{+}>GAL4, UAS-GFP; Frt82B, atg13$^{\Delta81}$scrib^{1}/Frt82B, tub-GAL80, atg13$^{\Delta81}$*

3f,g,h: *y,w,ey-FLP/y,w;UAS-Ras^{V12}/act>y^{+}>GAL4, UAS-GFP; Frt82B/Frt82B, tub-GAL80*

y,w,ey-FLP/y,w;UAS-Ras^{V12}/act>y^{+}>GAL4, UAS-GFP; Frt82B, scrib^{1}/Frt82B, tub- GAL80

y,w,ey-FLP/y,w;UAS-Ras^{V12}/act>y^{+}>GAL4, UAS-GFP; Frt82B, atg13$^{\Delta81}$scrib^{1}/Frt82B, tub-GAL80, atg13$^{\Delta81}$

y,w,ey-FLP/ ey3.5-Hsp70-DmAtg13-GFP;UAS-Ras^{V12}/act>y^{+}>GAL4, UAS-GFP; Frt82B, atg13$^{\Delta81}$scrib^{1}/Frt82B, tub-GAL80, atg13$^{\Delta81}$

3i,j: *y,w,ey-FLP/y,w;UAS-Ras^{V12}/act>y^{+}>GAL4, UAS-GFP; Frt82B, atg13$^{\Delta81}$scrib^{1}/Frt82B, tub-GAL80, atg13$^{\Delta81}$*

Figure 4.

4a: *y,w,ey-FLP/y,w;UAS-Ras^{V12}/act>y^{+}>GAL4, UAS-GFP; Frt82B/Frt82B, tub-GAL80*

y,w,ey-FLP/y,w;UAS-Ras^{V12}/ act>y$^+$>GAL4, UAS-GFP; Frt82B, scrib^1/Frt82B, tub-GAL80

4b: *y,w,ey-FLP/y,w;UAS-Ras^{V12}/ act>y$^+$>GAL4, UAS-GFP; Frt82B, scrib^1/Frt82B, tub-GAL80*

y,w,ey-FLP/y,w;UAS-Ras^{V12}/act>y$^+$>GAL4, UAS-GFP; Frt82B, atg13$^{\Delta81}$scrib^1/Frt82B, tub-GAL80, atg13$^{\Delta81}$

4c: *y,w,ey-FLP/y,w;UAS-Ras^{V12}/act>y$^+$>GAL4, UAS-GFP; Frt82B/Frt82B, tub-GAL80*

y,w,ey-FLP/y,w;UAS-Ras^{V12}/ act>y$^+$>GAL4, UAS-GFP; Frt82B, scrib^1/Frt82B, tub-GAL80

y,w,ey-FLP/y,w;UAS-Ras^{V12}/act>y$^+$>GAL4, UAS-GFP; Frt82B, atg13$^{\Delta81}$scrib^1/Frt82B, tub-GAL80, atg13$^{\Delta81}$

hsflp;;Frt82B, atg13$^{\Delta81}$/ Frt82B, atg13$^{\Delta81}$

hsflp;;Frt82B / Frt82B

Figure 5.

5a: *y,w,ey-FLP/y,w;UAS-Ras^{V12}/act>y$^+$>GAL4, UAS-GFP; Frt82B/Frt82B, tub-GAL80*

y,w,ey-FLP/y,w;UAS-Ras^{V12}/ act>y$^+$>GAL4, UAS-GFP; Frt82B, scrib^1/Frt82B, tub-GAL80

y,w,ey-FLP/y,w;UAS-Ras^{V12}/act>y$^+$>GAL4, UAS-GFP; Frt82B, atg13$^{\Delta81}$scrib^1/Frt82B, tub-GAL80, atg13$^{\Delta81}$

5b: *y,w,ey-FLP/y,w;UAS-Ras^{V12}/act>y$^+$>GAL4, UAS-GFP; Frt82B/Frt82B, tub-GAL80*

5c,d: *y,w,ey-FLP/y,w;UAS-Ras^{V12}/ act>y$^+$>GAL4, UAS-GFP; Frt82B, scrib^1/Frt82B, tub-GAL80*

5e: *y,w,ey-FLP/y,w;UAS-Ras^{V12}/act>y$^+$>GAL4, UAS-GFP; Frt82B, atg13$^{\Delta81}$scrib^1/Frt82B, tub-GAL80, atg13$^{\Delta81}$*

5g: *y,w,ey-FLP/y,w;UAS-Ras^{V12}/ act>y$^+$>GAL4, UAS-GFP; Frt82B, scrib^1/Frt82B, tub-GAL80*

Expanded View Figure 1.

EVF 1a: *y,w,ey-FLP/y,w;UAS-Ras^{V12} / act>y$^+$ >GAL4, UAS-GFP; Frt82B /Frt82B, tub-GAL80*

EVF 1b,c: *y,w,ey-FLP/y,w;UAS-Ras^{V12} / act>y$^+$ >GAL4, UAS-GFP; Frt82B, scrib^1 /Frt82B, tub-GAL80*

EVF 1d: *w^{1118}*

EVF 1e: *w^{1118}/w*, spok-Gal4, UAS-Dcr-2.D; UAS-rpr*

EVF 1f: *;;ecd^1, st^1, ca^1/ecd^1, st^1, ca^1* (Bloomington 218)

Expanded View Figure 2.

EVF 2a: *y,w,ey-FLP/y,w;UAS-Ras^{V12}, pmCh-atg8a/act>y$^+$>GAL4, UAS-GFP; Frt82B/Frt82B, tub-GAL80*

y,w,ey-FLP/y,w;UAS-Ras^{V12}, pmCh-atg8a/act>y$^+$>GAL4, UAS-GFP; Frt82B, scrib^1/Frt82B, tub- GAL80

y,w,ey-FLP/y,w;UAS-Ras^{V12}, pmCh-atg8a/act>y$^+$>GAL4, UAS-GFP; Frt82B, atg13$^{\Delta81}$scrib^1/Frt82B, tub-GAL80, atg13$^{\Delta81}$

EVF 2b: *y,w,ey-FLP/y,w;UAS-Ras^{V12}/act>y$^+$ >GAL4, UAS-GFP; Frt82B, atg13$^{\Delta81}$scrib^1/Frt82B, tub-GAL80, atg13$^{\Delta81}$*

EVF 2c: *y,w,ey-FLP/y,w;UAS-Ras^{V12}/act>y$^+$>GAL4, UAS-GFP; Frt82B/Frt82B, tub-GAL80*

y,w,ey-FLP/y,w;UAS-Ras^{V12}/act>y$^+$>GAL4, UAS-GFP; Frt82B, scrib^1/Frt82B, tub-GAL80

y,w,ey-FLP/y,w;UAS-Ras^{V12}/act>y$^+$>GAL4, UAS-GFP; Frt82B, atg13$^{\Delta81}$scrib^1/Frt82B, tub-GAL80, atg13$^{\Delta81}$

EVF 2d,e: *y,w,ey-FLP/y,w; g-atg13, UAS-Ras^{V12}/act>y$^+$>GAL4, UAS-GFP; Frt82B, atg13$^{\Delta81}$scrib^1/Frt82B, tub-GAL80, atg13$^{\Delta81}$*

EVF 2f: *y,w,ey-FLP/y,w;UAS-Ras^{V12}/act>y$^+$>GAL4, UAS-GFP; Frt82B, atg14$^{\Delta5.2}$,scrib^1/Frt82B, tub-GAL80, atg14$^{\Delta5.2}$*

EVF 2g: *y,w;;Frt82B, atg13$^{\Delta81}$/Frt82B, atg13$^{\Delta81}$*

y,w,ey-FLP/y,w;UAS-Ras^{V12}/act>y$^+$>GAL4, UAS-GFP; Frt82B, scrib^1/Frt82B, tub-GAL80

y,w,ey-FLP/y,w;UAS-Ras^{V12}/act>y$^+$>GAL4, UAS-GFP; Frt82B, atg14$^{\Delta5.2}$,scrib^1/Frt82B, tub-GAL80, atg14$^{\Delta5.2}$

Expanded View Figure 3.

EVF 3a: *y,w,ey-FLP/y,w;UAS-Ras^{V12}/act>y$^+$>GAL4, UAS-GFP; Frt82B, atg13^{Δ81}scrib^1/Frt82B, tub-GAL80, atg13^{Δ81}*

y,w,ey-FLP/y,w;UAS-Ras^{V12}/act>y$^+$>GAL4, UAS-GFP; Frt82B, scrib^1/Frt82B, tub-GAL80

EVF 3b: *y,w,ey-FLP/y,w;UAS-Ras^{V12}/act>y$^+$>GAL4, UAS-GFP; Frt82B, atg13^{Δ81}scrib^1/Frt82B, tub-GAL80, atg13^{Δ81}*

y,w,ey-FLP/y,w;UAS-Ras^{V12}/act>y$^+$>GAL4, UAS-GFP; Frt82B/Frt82B, tub-GAL80

EVF 3c: *y,w,ey-FLP/y,w;UAS-Ras^{V12}/act>y$^+$>GAL4, UAS-GFP; Frt82B/Frt82B, tub-GAL80*

y,w,ey-FLP/y,w;UAS-Ras^{V12}/act>y$^+$>GAL4, UAS-GFP; Frt82B, scrib^1/Frt82B, tub-GAL80

y,w,ey-FLP/y,w;UAS-Ras^{V12}/act>y$^+$>GAL4, UAS-GFP; Frt82B, atg13^{Δ81}scrib^1/Frt82B, tub-GAL80, atg13^{Δ81}

EVF 3d: *y,w,ey-FLP/y,w;UAS-Ras^{V12}/act>y$^+$>GAL4, UAS-GFP; Frt82B/Frt82B, tub-GAL80*

y,w,ey-FLP/y,w;UAS-Ras^{V12}/act>y$^+$>GAL4, UAS-GFP; Frt82B, scrib^1/Frt82B, tub-GAL80

y,w,ey-FLP/y,w;UAS-Ras^{V12}/act>y$^+$>GAL4, UAS-GFP; Frt82B, atg13^{Δ81}scrib^1/Frt82B, tub-GAL80, atg13^{Δ81}

Expanded View Figure 4.

EVD 4a: *y,w,ey-FLP/y,w;UAS-Ras^{V12}/act>y$^+$>GAL4, UAS-GFP; Frt82B, scrib^1/Frt82B, tub-GAL80*